Energy Storage Materials 25 (2020) 52–61

Contents lists available at ScienceDirect

Energy Storage Materials

journal homepage: www.elsevier.com/locate/ensm

Surface engineering donor and acceptor sites with enhanced charge transport for low-overpotential lithium–oxygen batteries

Shu-Mao Xu [a], Xiao Liang [a], Xin Liu [a], Wen-Long Bai [a], Yu-Si Liu [a], Zhi-Peng Cai [a], Qiang Zhang [a], Chuan Zhao [b], Kai-Xue Wang [a,*], Jie-Sheng Chen [a,**]

[a] School of Chemistry and Chemical Engineering, Shanghai Jiao Tong University, Shanghai, 200240, China
[b] School of Chemistry, University of New South Wales, Sydney, 2052, Australia

ARTICLE INFO

Keywords:
Lithium-oxygen batteries
Electron transfer
Low overpotential
Defective charge transport
Donor acceptor sites

ABSTRACT

Inferior charge transport in discharge products is one of the main factors restricting the technological potential of lithium-oxygen batteries. Here, we propose a strategy to enhance charge transport in discharge products by surface engineering of cathode catalysts with donor and acceptor sites to improve solid-solid interfacial electron transfer properties between catalysts and discharge products. Free-standing layered double oxides loaded with pyrolyzed sodium poly(aminobenzenesulfonate)-derived sulfur-doped carbon nanosheets and carbon nanosheets with sulfoxide groups are synthesized and utilized to investigate donor and acceptor sites effect on the performance of lithium-oxygen batteries. The free-standing cathode with hybrid donor and acceptor sites is capable of operation in oxygen with distinct (dis)charge plateau and superior cycling stability (over 60 cycles at a fixed capacity of 0.53 mAh cm^{-2}). The superior properties are attributed to the enhanced charge transport in lithium peroxide by the formation of hole polarons/Li^+ vacancies on acceptor sites and electron polarons/disordered lithium peroxide phase on donor sites. This work provides a promising route to enhance defective charge transport in discharge products by optimization of donor and acceptor sites on cathode catalysts for high-performance lithium-oxygen batteries.

1. Introduction

Aprotic Li–O_2 batteries (LOBs) have attracted intense interest because of their high theoretical energy density, which considerably exceeds that of current Li-ion batteries [1–5]. Upon discharge in typical aprotic Li–O_2 batteries, O_2 is reduced on the cathode surface to form intermediate LiO_2*, which then undergoes either chemical disproportionation or continuous electrochemical reduction to form Li_2O_2 [1,2,6]. Crystalline Li_2O_2 is an insulator with theoretical band gap of 4.9 eV [7,8], whose conductivity at room temperature is only 10^{-12}–10^{-13} S cm^{-1} [9–11]. During discharge, the activated sites on the catalyst surface were quickly covered by insulative Li_2O_2, which would cause the passivation of the air electrode and the "sudden death" of the battery with limited discharge capacity and rapid voltage drop [12,13]. The subsequent electrochemical reaction on the surface of Li_2O_2 discharge products with inferior charge transport is usually a major factor restricting the kinetics of oxygen reduction and evolution and thus leading to the high overpotential of Li–O_2 batteries. Theoretical calculation revealed that the introduction of additional electron for donor doping in Li_2O_2 crystal with small electron polarons of localized O_2^{3-} as charge carriers [14–16], or the removal of electron/Li from crystal Li_2O_2 for p-doping with small hole polarons [17,18] or Li vacancies [7,19] as charge carriers would significantly enhance charge transport in Li_2O_2. Therefore, the development of cathode catalysts with optimized surface/interface structures to enhance interfacial electron transfer properties and the charge transport in discharge products is of great significance to lower the overpotential of Li–O_2 batteries.

Noble metal catalysts with superior catalytic activity towards Li_2O_2 decomposition were found to be associated with the kinetics of the charge reaction between solid noble catalysts and solid discharge products by electrochemical mass spectrometry [20]. Bimetallic catalysts, such as Pd-Cu [21], and Pt–Cu [22,23], were reported to exhibit lower (dis)charge overpotentials than original noble metal catalysts. The enhanced electron transfer from the transition metal atoms to noble metal atoms would decrease the adsorption strength of LiO_2*

* Corresponding author.
** Corresponding author.
E-mail addresses: k.wang@sjtu.edu.cn (K.-X. Wang), chemcj@sjtu.edu.cn (J.-S. Chen).

https://doi.org/10.1016/j.ensm.2019.10.032
Received 29 July 2019; Received in revised form 15 October 2019; Accepted 30 October 2019
Available online 4 November 2019

intermediates on the noble metal surface. Lu et al. [24] prepared Ag clusters with controlled sizes (Ag_3, Ag_9, Ag_{15}) on carbon surface and found that the morphologies of discharge products and the performance of Li–O_2 batteries varied with different Ag cluster sizes. These differences were attributed to different oxygen reduction activities of Ag clusters with different electron transfer properties to Li_2O_2 discharge products. For non-precious metal oxides catalysts towards Li_2O_2 decomposition, an interfacial model involving Co_3O_4 (111) and Li_2O_2 constructed by density functional theory (DFT) calculation indicated that the high catalytic activity of O-rich Co_3O_4 (111) in reducing O_2 desorption barrier and the charge overpotential was originated from the fast electron transfer from the Li_2O_2 layer to the underlying catalyst surface [25]. In addition, the electron transport property of metal oxide catalysts enhanced by nitridation was demonstrated to effectively lower the overpotential of Li–O_2 batterie [26].

Heteroatom doping in carbon materials is another effective approach extensively utilized to regulate the electronic structure of carbon catalysts in Li–O_2 batteries. Pyridinic-N-doped graphene was reported to be more effective for promoting the nucleation of Li_2O_2 clusters than pristine or graphitic-N-doped graphene [27–29], owing to the enhanced electron transfer from Li_2O_2 discharge products to the pyridinic-N sites. P-doped and B-doped graphene materials were also reported to exhibit high catalytic activity in reducing the (dis)charge overpotential [30,31]. However, owing to the lack of suitable catalysts for donating and accepting electron with LiO_2*/Li_2O_2 in Li–O_2 batteries, clear illustration of the effect of electron transfer between catalyst and discharge products on the properties of Li_2O_2 and the performance of Li–O_2 batteries has not been established.

Based on DFT simulation, the electron donating and accepting effect on the properties of Li_2O_2 is shown to be tunable by regulating different sulfur sites on carbon support. The adsorption of LiO_2*/Li_2O_2 molecules on thiapyridine (S1) and sulfoxide (S2) sites is accompanied with electron transfer from S1 and S2 sites to LiO_2*/Li_2O_2, while that on thioether (S3) and polysulfide (S4) sites is accompanied with electron transfer from adsorbates to S3 and S4 sites. S2 sites could generate through the incomplete decomposition of sulfonate groups at relatively low temperature, while S3 and S4 sites would form during carbonization over 700 °C.

Herein, the manipulation of acceptor and donor sites upon adsorbing LiO_2*/Li_2O_2 in Li–O_2 batteries is realized by pyrolysis of sodium poly (aminobenzenesulfonate) (PABSA) at different temperatures. To avoid side reactions induced by the polymer binder and the conductive carbon additive, a binder-free cathode with layered double oxides (LDO) nanoflake arrays is prepared and employed to load with PABSA. Successive carbonization at different temperatures leads to the formation of composites (PABSA/LDO-n, n: carbonization temperature) composed of LDO loaded with pyrolyzed poly (aminobenzenesulfoni)-derived carbon nanosheets with different S sites. Upon discharge, particles-like discharge products are generated on PABSA/LDO-600, while flakey discharge products are found well dispersed on PABSA/LDO-700. The difference in the morphology of discharge products might be associated with different preferential adsorption and coverage of reactants and intermediates on the donor and acceptor sites. This work sheds light on rational construction of cathode catalyst with optimized donor and acceptor sites to tailor deposition of Li_2O_2 with enhanced defective charge transport for low-overpotential Li–O_2 batteries.

2. Experimental section

Electrodeposition of CoTi LDH: 0.21 mL $TiCl_4$ was added dropwise to 40 mL of 0.023 g mL^{-1} $Co(NO_3)_2$ aqueous solution (Co:Ti molecular ratio of 3:1) to form homogeneous solution under vigorous stirring. After ultrasonic dispersion for 30 min, 0.74 mL of concentrated ammonia (28 wt %) was added dropwise into the above solution under vigorous stirring. At a constant potential of −2.0 V (vs SCE), CoTi LDH was electrodeposited onto the nickel foam for 600 s in the above electrolyte with Pt foil as counter electrode. The CoTi LDH generated on the nickel foam was rinsed twice with deionized water and then anhydrous ethanol, dried for 6 h at 60 ºC. The as-obtained CoTi LDH was calcined at 200 ºC in air for 2 h to form CoTi LDO.

Preparation of PABSA/LDO: CoTi LDO on nickel foam was added to 80% alcoholic aqueous solution containing sodium m-aniline sulfonate, in a molar ratio of organic anion: LDO = 4:1. After reacted at 70 °C for 10 h, the samples were rinsed twice with deionized water and then anhydrous ethanol. After dried at 60 °C for 5 h and annealed at 300 °C (5 °C min^{-1} to 200 °C; 1 °C min^{-1} from 200 to 300 °C) in N_2 for another 0.5 h, sodium poly (aminobenzenesulfonate) was prepared. The carbonization of the composites is calcined at 600 °C, 700 °C and 800 °C for 2 h under N_2. For comparison, PAN/LDO-700 was prepared by using aniline monomer as the carbon and nitrogen sources after calcination at 700 °C. The obtained final product was used directly as binder-free electrodes for Li–O_2 batteries.

Structural characterization: The X-ray diffraction (XRD) patterns were recorded on a D/Max 2550VL/PC X-ray diffractometer (Rigaku, Japan) equipped with Cu K_α radiation ($\lambda = 1.5418$ Å, 40 kV, 30 mA). Fourier transform infrared spectroscopy (FTIR) was measured on a Spectrum 100, PerkinElmer using the KBr disk. X-ray photoelectron spectroscopy (XPS) was performed on an AXIS ultra DLD spectrometer (Kratos, Japan) with Al K_α radiation ($h\nu = 1486.6$ eV). The morphology of the samples was observed using a field-emission scanning electron microscope (FESEM) (FEI Nova Nano SEM 230, USA). The transmission electron microscopy (TEM) and high-resolution transmission electron microscopy (HRTEM) observations were carried out on a JEM-2100F microscope operated at an acceleration voltage of 200 kV. HAADF-STEM characterization was carried out on JEM-ARM200F (JEOL, Tokyo, Japan). TEM/STEM operated at 200 kV with cold filed-emission gun and aberration corrector. Time-of-flight secondary ion mass spectrometry (TOF-SIMS) and TOF-SEM were carried out on a TESCAN Gaia 3 FESEM. The X-ray absorption (XAFS) data at the Co and N K-edge of the samples were recorded at room temperature in transmission mode using ion chambers (referenced samples) and fluorescence excitation mode using a Lytle detector (controlled samples) at beamline BL14W1 of the Shanghai Synchrotron Radiation Facility. The station was operated with a Si (111) double crystal monochromator. During the measurement, the synchrotron was operated at 3.5 GeV and the current was controlled between 150 and 210 mA. The data for each sample were calibrated with standard Co metal foil. Data processing was performed using the program ATHENA. Extended X-ray absorption fine structure (EXAFS) spectra were fitted using the FEFF 7.0 code.

Assembling Li–O_2 batteries: The electrochemical performance was analyzed using CR2025-type Swagelok coin cell. All of the cells were assembled in a glove box filled with ultra-highly pure Ar using millipore glass fiber membrane as the separator, lithium metal foil as anodes and 1 M LiTFSI in TEGDME as the electrolyte. The diameter of the electrode is 12 mm.

Electrochemical measurement: The galvanostatic charge and discharge experiment was performed with a battery tester (LAND CT2001A). The full discharge and charge were limited in the potential range of 2.25–4.2 V at room temperature with a current density of 100 mA g^{-1} (normalized to the total weight of catalyst). The cycling of PABSA/LDO-700 and PAN/LDO-700 is fixed at a capacity of 0.53 and 0.35 mAh cm^{-2}, respectively. Pretreatment of the binder-free cathodes was conducted by cycling the battery between 2.25 and 4.2 V for 10 cycles. Cyclic voltammetry (CV) was performed on the Auto Lab workstation at a scanning rate of 0.2 mV s^{-1} in a potential range of 2.25–4.2 V (vs Li/Li^+). All the batteries were equilibrated at open circuit for 10 h before testing. For the plots of *dQ/dV*, relative infinity points corresponding to platform capacity are removed.

DFT calculations: First-principle calculations were performed by the density functional theory (DFT) using the Vienna *ab*-initio simulation package (VASP) package [32,33]. The generalized gradient approximation (GGA) with the Perdew-Burke-Ernzerhof (PBE) functional was used

to describe the electronic exchange and correlation effects. Uniform G-centered k-points meshes with a resolution of $2\pi \times 0.03\,\text{Å}^{-1}$ and Methfessel-Paxton electronic smearing were adopted for the integration in the Brillouin zone for geometric optimization. The simulation was run with a cutoff energy of 500 eV throughout the computations. These settings ensure convergence of the total energies to within 1 meV per atom. Structure relaxation proceeded until all forces on atoms were less than 1 meV Å^{-1} and the total stress tensor was within 0.01 GPa of the target value.

3. Results and discussion

3.1. Structural analysis of the cathode catalysts

The typical preparation procedure for PABSA/LDO composites is shown in Fig. 1a. CoTi layered double hydroxides (LDH) nanoflake arrays with intercalated nitrate were first uniformly grown onto nickel foam by an electrodeposition method [34]. Driven by the electrostatic interaction, metanilic monomers were intercalated into the interlayers of positively charged LDH, leading to the formation of ABSA/LDH precursors. Successive polymerization was achieved by oxidation of interlayer-confined metanilic monomers with the decomposition of pre-intercalated nitrate as an oxidizing agent at 300 °C, generating PABSA/LDO-300 composites. Without LDO nanoflake supports, the direct polymerization of metanilic monomers on Ni foam would lead to the formation of one-dimensional rod-like instead of two-dimensional nanosheet products (Fig. S1). PABSA/LDO-300 was pyrolyzed at 600 °C, 700 °C and 800 °C, generating PABSA/LDO-600, PABSA/LDO-700 and PABSA/LDO-800 composites, respectively composed of carbon nanosheets with different S sites. For comparison, a composite composed of N-doped carbon and LDO without S sites (PAN/LDO-700) was prepared by calcination of LDH nanoflakes with aniline monomers at 700 °C.

Scanning electron microscopic (SEM) images of the as-synthesized samples are shown in Fig. 1b–d. LDH nanoflake arrays were successfully deposited onto Ni foam (Fig. 1b). The nanoflakes of PABSA/LDO-300 (Fig. 1c) is thicker than those of ABSA/LDH, suggesting the formation of polymer coatings on pristine nanoflakes. The characteristic shape-up satellite peak located at 292.2 eV in C 1s X-ray photoelectron

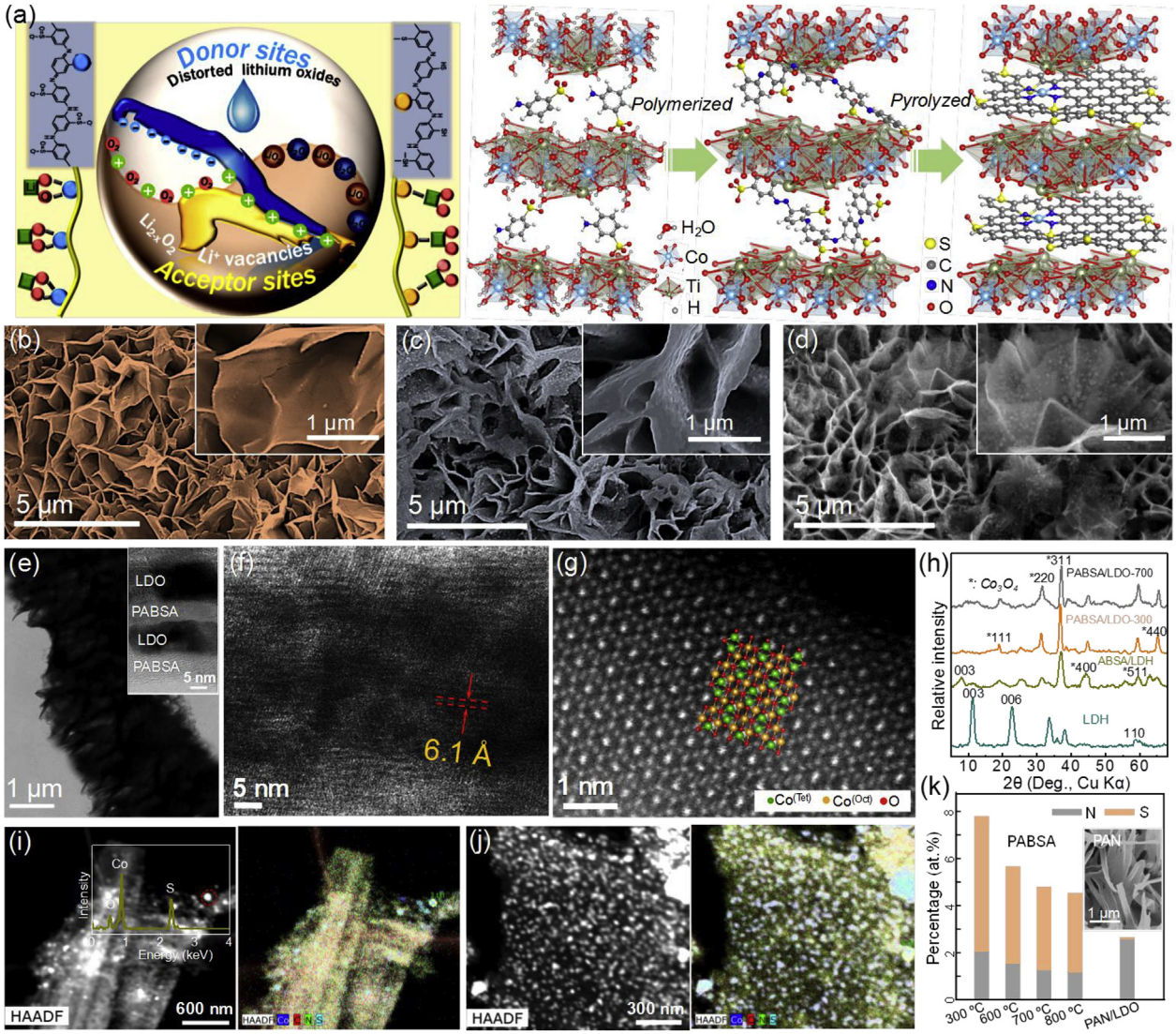

Fig. 1. (a) Scheme for regulating different sulfur sites for constructing donor and acceptor sites on catalyst surface. SEM images of (b) ABSA/LDH, (c) PABSA/LDO-300 and (d) PABSA/LDO-700. TEM images of (e) PABSA/LDO-300 nanoflake and (f) PABSA/LDO-700. Insets in b-e are the corresponding enlarged images. (g) ADF-STEM image of PABSA/LDO-700. The color spheres represent O (red), Co^{3+} of oxygen octahedral sites (orange) and Co^{2+} of oxygen tetrahedral sites (green). (h) XRD patterns of precursor and PABSA/LDO derivatives. HAADF-STEM and elemental images of (i) PABSA/LDO-700 nanoflakes and (j) carbon nanosheet. (k) N, S contents of different samples. Inset is the SEM image of PAN/LDO-700. (For interpretation of the references to color in this figure legend, the reader is referred to the Web version of this article.)

spectroscopic (XPS) spectrum of PABSA/LDO-300 attributed to the π-π* transition in aromatic rings with extended delocalized electrons revealed the polymerization of metanilic monomer in PABSA/LDO-300 (Fig. S2). The polymerization is further demonstrated by the characteristic -C-N stretching vibration in the infrared (IR) spectrum of PABSA/LDO-300 (Fig. S2). After calcination, the flake-like morphology of PABSA/LDO-700 is well maintained (Fig. 1d). Different from the smooth surface of ABSA/LDH, the surface of PABSA/LDO-700 nanoflakes is decorated with plenty of particles. Transmission electron microscopic (TEM) observation shows that LDO flakes with thickness of ~10 nm are separated regularly by PABSA polymers (Fig. 1e). After carbonization at 700 ℃, disordered layered fringes are observed, indicating the partial destruction of layered structure of PABSA/LDO-700 (Fig. 1f). Further observation by annular dark field scanning transmission electron microscopy (ADF-STEM) with atomic resolution shows the Co columns of Co_3O_4 (*l*00) plane in PABSA/LDO-700 (Fig. 1g). The layered spacing of PABSA/LDO-700 calculated based on the peak centered at 12.8° in X-ray diffraction (XRD) pattern is ~6.9 Å, while that of ABSA/LDH and PABSA/LDO calculated based on (003) diffraction peaks is 11.1 and 10.8 Å, respectively (Fig. 1h). The high-angle annular dark-field STEM (HAADF-STEM) observation reveals that nanoparticles with average size of ~25 nm are well dispersed in LDO nanoflakes and carbon nanosheet of PABSA/LDO-700 (Fig. 1i and j). Elemental mapping indicates that these particles are mainly composed of Co, S and O. Further observation by HRTEM demonstrates the existence of Co_3O_4 and S phase in these nanoparticles (Fig. S3). The atomic ratio of S in PABSA/LDO-300 is ~5.7 at% (Fig. 1k). The contents of S in the samples decrease gradually with the increase of calcination temperatures (~4.07, 3.48 and 3.31 at% in PABSA/LDO-600, PABSA/LDO-700 and PABSA/LDO-800, respectively) (Table S1). Sulfonate groups in metanilic acid monomer can be completely decomposed at 600 ℃ [35]. During the carbonization of the composites at 700 ℃, the colorless aqueous solution in a bottle connected to the vent of the tube furnace turns yellow, suggesting the formation of polysulfide during pyrolysis of PABSA (Fig. S4). The π* resonance at 397 eV in N K-edge X-ray absorption near-edge structure (XANES) spectra reveal that N mainly exists as pyridinic N in PABSA/LDO-700 (Fig. S5).

The adsorption of O_2, LiO_2*, and Li_2O_2 on different S active sites was simulated by DFT calculation (Fig. 2a). The charge difference density (CDD) profiles of O_2, LiO_2*, and Li_2O_2 adsorbed on different S sites and Co–N sites were shown in Fig. 2b and c. As indicated by the electron accumulation around O, chemical bonds with O in LiO_2*/Li_2O_2 might form for Co–N, S1 and S2 sites. However, S3 and S4 sites are prone to bond with Li in LiO_2*/Li_2O_2. The O–O bond length of LiO_2* adsorbed on S3 and S4 sites is similar with that of original LiO_2* (1.34 Å). After adsorbing LiO_2*, the corresponding O–O bond lengths of LiO_2* on S1 and S2 sites increase to 2.99 and 2.32 Å, respectively, indicating the large distortion of LiO_2* on S1 and S2 sites (Fig. 2b and Fig. S6). Analogous with LiO_2*, Li_2O_2 adsorbed on S1 and S2 sites also shows larger distortion than that on other sites (Fig. 2c). The bonding characteristics of the cluster model adsorbing reactive oxygen species were further evaluated by CDD profiles projected on the selective bonding planes. The S2 site prefers to bond with two O atoms from LiO_2* (Fig. 2b). When adsorbing Li_2O_2, the initial O in sulfoxide bonding with Li would locate in the same plane with Li (1), Li (3) and O (4) of Li_2O_2, while the S2 site and O (2) of Li_2O_2 protrude out of the plane (Fig. 2c). However, when adsorbing LiO_2*/Li_2O_2, the S3 and S4 sites prefer to bond with electron-donating Li in lithium oxides instead of O (Fig. 2b,c and Fig. S6). The coupling interaction between different S sites and reactive oxygen species can be further quantitatively evaluated by Bader charge transfer analyses [36, 37]. Fig. 2d shows the change of valence state of different S sites upon adsorbing O_2, LiO_2*/Li_2O_2. Upon adsorption of O_2, LiO_2*/Li_2O_2, the valence charges of S1 and S2 sites increase, suggesting the loss of electrons from S1 and S2 sites. On the contrary, the valence charges of S3 and S4 sites decreases when adsorbing LiO_2*/Li_2O_2, indicative of the gain of electrons on these sites. The total electron transfer for O_2, LiO_2*/Li_2O_2 adsorbed on different sites is shown in Fig. 2e. Upon adsorbing O_2,

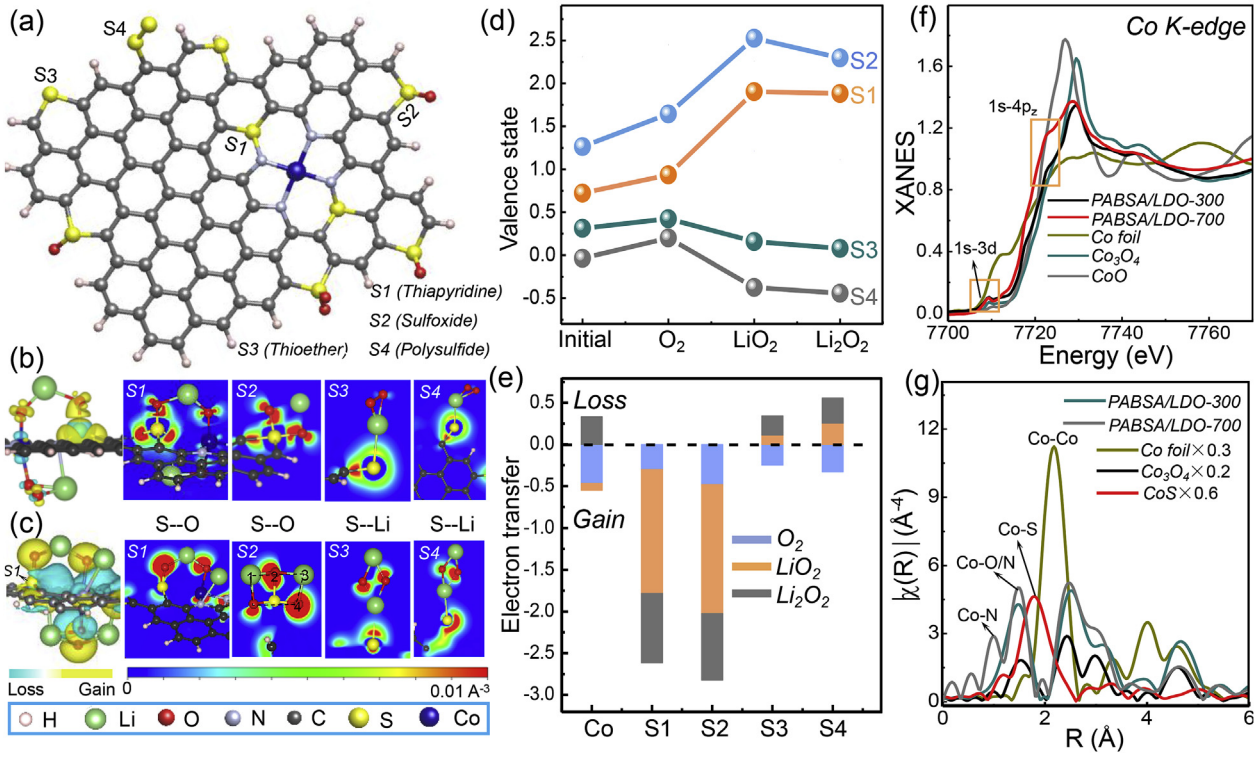

Fig. 2. (a) The cluster model for adsorption of O_2, LiO_2*/Li_2O_2. Selective charge difference density profiles of (b) LiO_2* and (c) Li_2O_2 on S1, S2, S3 and S4 sites. LiO_2*/Li_2O_2 are prone to dissociate with large distortion on S1 and S2 sites. (d) Valence state of different S sites based on Bader charge upon adsorption of O_2, LiO_2*/Li_2O_2. (e) The total electron transfer for O_2, LiO_2*/Li_2O_2 adsorbed on different sites. (f) Co K-edge X-ray absorption near-edge structure (XANES) and (g) Fourier transformed extended X-ray absorption fine structure of PABSA/LDO-300 and PABSA/LDO-700.

electrons transfer from the substrate cluster to O_2. For LiO_2*, gain of electron occurs on Co–N, S1 and S2 sites, while loss of electron occurs on S3 and S4 sites. The electron transfer tendency for Li_2O_2 adsorbed on different sites is similar with that of LiO_2* except for Co–N sites where electron donating instead of gaining occurs. Therefore, S1 and S2 sites are classified as "donor sites" with electron donation to adsorbates, while S3 and S4 sites are classified as "acceptor sites" with electron transferring from adsorbates to these sites. LiO_2*/Li_2O_2 adsorbed onto donor sites tend to dissociate with large distortion. It is consistent with the DFT-HSE (Heyd Scuseria Ernzerhof) calculation results reported by Radin et al. [12] that injection of an extra electron in Li_2O_2 crystal will result in the structure distortion of Li_2O_2 with elongation of O–O bond length and eventually lead to the break of O–O bond.

Co K-edge XANES spectra of PABSA/LDO-300 and PABSA/LDO-700 with Co foil, CoO, and Co_3O_4 as references suggest the similar valence of Co in the composites with that of Co_3O_4 (Fig. 2f). The magnitude of Fourier transform (FT) EXAFS spectrum of PABSA/LDO-300 closely resembles that of Co_3O_4 reference (Fig. 2g). However, the shoulder in the first coordination shell of PABSA/LDO-700 shows more resemblance to cobalt phthalocyanine [38,39], suggesting the existence of Co–N configuration in PABSA/LDO-700. XANES simulation of various DFT-optimized architectural models was further carried out to investigate the local geometric structure and ligand environment around Co sites (Figs. S7 and 8). The bond length of the neighboring coordination of Co in the constructed adsorption model is well matched with experimental XAFS characterization of PABSA/LDO-700 (Table S3). The S 2p XPS spectrum of PABSA/LDO-300 and PABSA/LDO-600 (Fig. 3a) exhibited a peak centered at 168.6 eV, ascribed to the S–O bonds in sulfonate [40]. After carbonization at 700 ºC, a new peak corresponding to C–S band appeared at lower energy (163.3 eV) [41], suggesting the incorporation of S into carbon nanosheets. The existence of C–S peak in PABSA/LDO-700 and PABSA/LDO-800 demonstrates the successful doping of S into carbon with S3 and S4 acceptor sites in PABSA/LDO-700 and PABSA/LDO-800. However, no characteristic C–S peak is observed in S 2p XPS spectrum of PABSA/LDO-600, indicating the absence of S3 and S4 acceptor sites in PABSA/LDO-600.

4. Electrochemical properties of PABSA/LDO cathode

The electrochemical properties of PABSA/LDO as bifunctional catalysts for oxygen electrodes were evaluated at constant rate of 26.5 μA cm^{-2} (Fig. 3b–e). At a cutoff voltage of 2.25 V, PABSA/LDO-300, PABSA/LDO-600, PABSA/LDO-700 and PABSA/LDO-800 deliver initial specific discharge capacities of 92.5, 992, 3092 and 1486 mAh g^{-1}, respectively (Fig. 3b,c and Figs. S9 and 10). Both PABSA/LDO-300 and PABSA/LDO-600 exhibit distinct kinetic overpotential with delayed voltage response at the start of discharge profiles and linear voltage variation in the deep discharge (Fig. 3b and c), while PABSA/LDO-700 and PABSA/LDO-800 exhibit slope-like profiles in the deep discharge (Figs. S9 and 10). The hysteresis in the response of voltage to time at the start of discharge profiles is often observed in many LOB catalysts in the successive cycles [42–44], which might be closely associated with the Li^+/e diffusion in solid or quasi-solid discharge products. The linear decrease of voltage could be observed in the deep discharge profiles of Ir-decorated reduced graphene oxides (Ir/GO) [45], glassy carbon [10], or branched carbon nanofibers [46]. Viswanathan et al. [10] proposed a metal-insulator-metal charge transport model to probe the electron transfer through Li_2O_2 film on glassy carbon cathode and ascribed the above linear voltage drop to the ohmic polarization induced by the inhibition of charge transport on Li_2O_2 discharge products. In deep discharge, the surface of catalyst is completely covered by discharge products. The polarization in deep discharge might be mainly originated

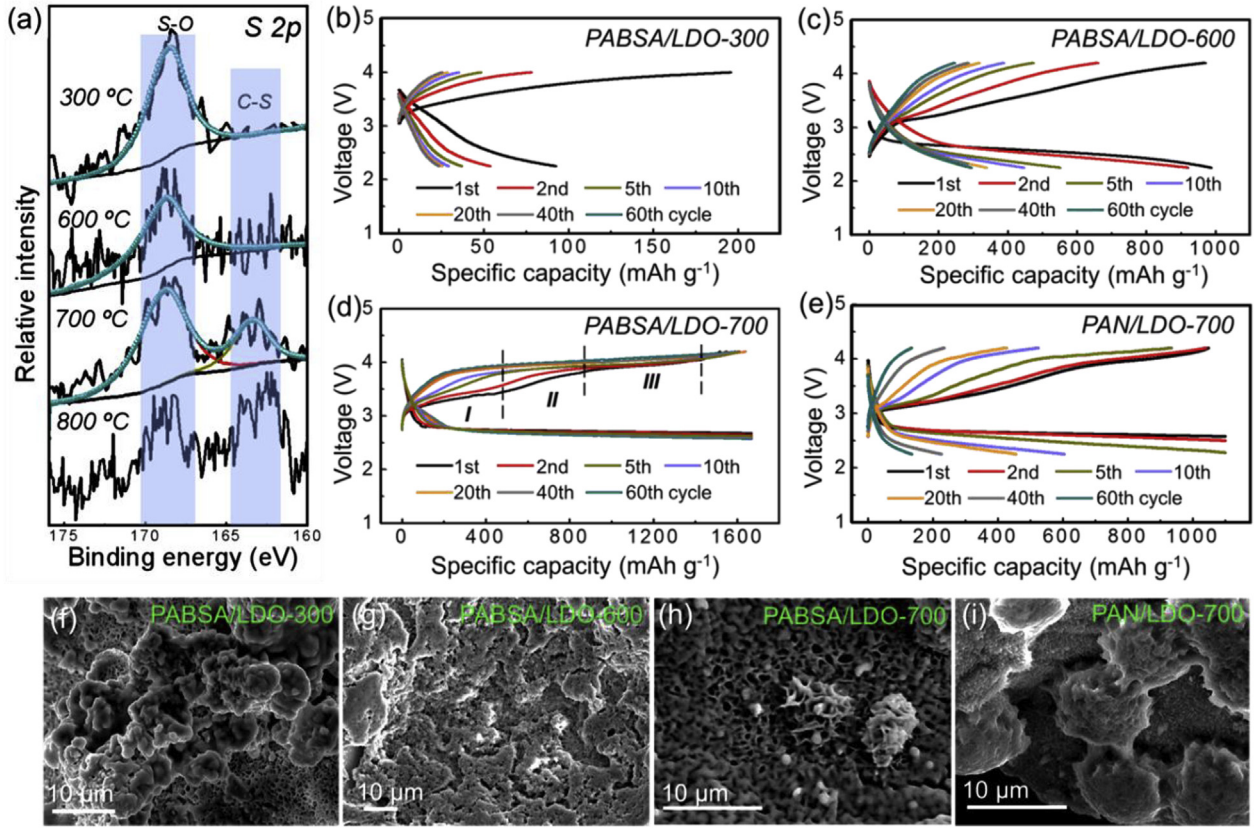

Fig. 3. (a) S 2p XPS spectra of PABSA/LDO at different temperatures. Selective (dis)charge curves of (b) PABSA/LDO-300, (c) PABSA/LDO-600, (d) PABSA/LDO-700, and (e) PAN/LDO-700 at 26.5 μA cm^{-2}. SEM images of discharged products on first discharged (f) PABSA/LDO-300, (g) PABSA/LDO-600, (h) PABSA/LDO-700, and (i) PAN/LDO-700.

from ohmic polarization. Relative derivation of dynamic equations further revealed the relationship between linear voltage variation and the disproportionation of LiO_2* on the catalyst surface [47].

The cycles of PABSA/LDO-700 are quite limited with significant capacity decay in the voltage range of 2.25–4.2 V (Fig. S9). At a fixed capacity of 0.53 mAh cm^{-2} (E > 2.6 V vs Li/Li^+), PABSA/LDO-700 shows superior cycling stability (Fig. 3d). The initial charge profile of PABSA/LDO-700 at a fixed capacity of 0.53 mAh cm^{-2} exhibits typical three regions characterized by distinct difference in slope (Fig. 3d). The charge voltage plateau at low voltage (~3.3 V vs Li/Li^+) is associated with the oxidation of superoxide-like phase on the surface of Li_2O_2 [26,48]. The solid solution delithiation forms off-stoichiometric $Li_{2-x}O_2$ [49,50], generating a slope-like charge profile. The following oxidation of crystalline Li_2O_2 cores with insulating property gives a charge plateau at ~4 V. For comparison, PAN/LDO-700 without S sites was cycled at a fixed capacity of 0.35 mAh cm^{-2} with initial discharge cutoff voltage of 2.6 V. Although low overpotential is observed in the initial two cycles, significant increase in the charge overpotential can be observed in the successive cycles (Fig. 3e).

The capacity and the cyclability of the Li–O_2 batteries are closely associated with the morphologies and crystal structure of Li_2O_2. To illustrate the variation in the performance of PABSA/LDO-derived

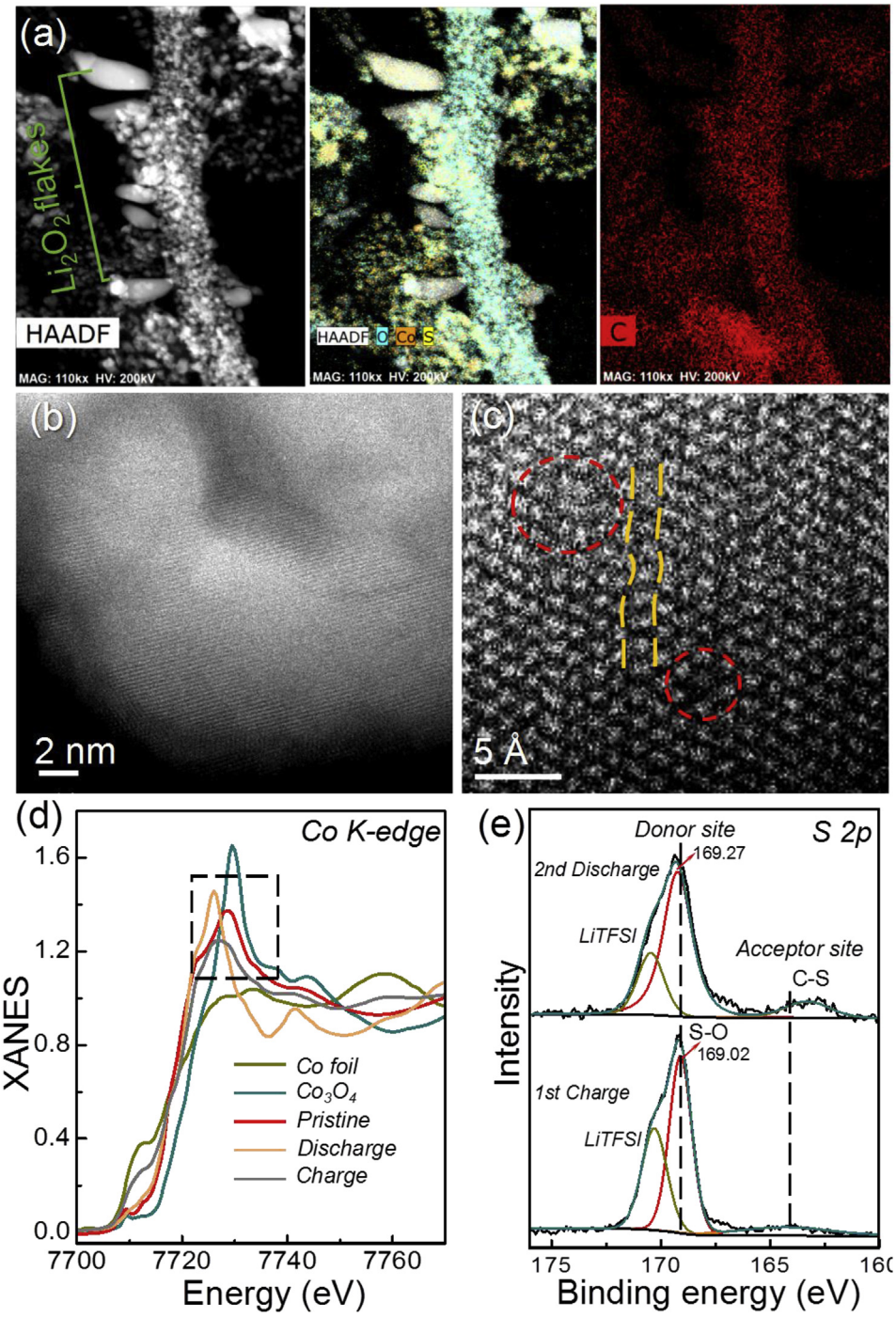

Fig. 4. (a) Elemental mapping images of first fully discharged PABSA/LDO-700 cathode. (b,c) Cs-corrected STEM images of disc discharge products. (d,e) Co K-edge XANES and S 2p XPS spectra of (dis)charged PABSA/LDO-700.

composites, morphologies of initial discharge products on cathodes surface were investigated by SEM and TEM. SEM observation shows that irregular spherical particles in micron size are attached on the surface of the discharged PABSA/LDO-300 electrode (Fig. 3f). The surface of discharged PABSA/LDO-600 is almost completely covered with film-like coatings composed of small particles (Fig. 3g). The full coverage of discharge products on the surface of discharged PABSA/LDO-600 might lead to the pronounced kinetic overpotential in the successive cycles. For discharged PABSA/LDO-700, small spherical particles are observed generated within the voids among the nanoflakes (Fig. 3h). However, large spherical particles in micron size are also observed scattering on the surface of the initial discharged PAN/LDO-700 (Fig. 3i and Fig. S11). TEM observation of discharged PABSA/LDO-600 further shows that small particles in average size of ~30 nm and large granules in micron size are generated and dispersed on the cathode surface (Fig. S12a). Some granules show a core-shell structure with amorphous shell and crystalline core. Distinct lattice fringes observed in the core are attributable to the (002) plane of Li_2O_2. For PABSA/LDO-700 cathode with hybrid donor and acceptor sites, flaky discharge products can be observed attached on the PABSA/LDO nanoflakes and small particles can be observed well dispersed and embedded onto the electrode surface (Fig. 4a). Further observation of these small particles by HRTEM shows distinct lattice fringe with spacings of approximately 2.2 Å, attributable to the (102) plane of Li_2O_2 (Figs. S13 and 14). Fast Fourier transformed (FFT) patterns of the disc discharge products and the substrate catalyst show the epitaxial growth of Li_2O_2 on (400) plane of Co_3O_4 (Fig. S14). The common superlattice of (102) plane of Li_2O_2 and (400) plane of Co_3O_4 has a small mismatch in both lateral dimensions, indicative of a translational symmetry beneficial for epitaxial growth over large distances. The distribution and properties of discharge products on PABSA/LDO-700 electrode are further demonstrated by time-of-flight (TOF)-secondary ion mass spectrometric (SIMS)-SEM analyses using Ga^+ sputtering (Fig. S15). The positive ion depth profiles of the discharged PABSA/LDO-700 cathode show that Li_3O^+ fragment has penetrated deeply into the surface, indicative of the formation of main discharge products of Li_2O_2. Further observation of discharge products by Cs-corrected STEM reveals the presence of vacant sites and structure distortion in disc-like Li_2O_2 (Fig. 4b and c) and amorphous phase in flaky discharge products (Fig. S16). Compared with crystalline Li_2O_2 with low electronic conductivity [9–11], defects, such as amorphous phase, lattice distortion and Li vacancies are believed to enhance charge transport in Li_2O_2. PABSA/LDO-700 electrode with better catalytic activity for Li_2O_2 formation and decomposition than PABSA/LDO-600 might be induced by the generation of abundant defects in discharge products with enhanced charge transport.

5. Electron transfer effect on the properties of discharge products

After discharge, the white line of Co K-edge of the discharged PABSA/LDO-700 shifts to lower energy suggesting the partial reduction of Co (Fig. 4d). After charge, the absorption edge shifts back to higher energy suggesting the oxidation of Co during charge. The shift of the characteristic S–O and C–S peaks in the S 2p XPS spectrum of the 2nd discharged PABSA/LDO-700 is obvious. The shift of S–O peak to higher binding energy indicates the loss of electron for S–O groups, while the shift of C–S peak to lower binding energy suggests the gain of electron for C–S groups during discharge (Fig. 4e). The blue shift of the S–O peak after discharge can also be observed in S 2p XPS spectra of (dis)charged PABSA/LDO-600 (Fig. S17). XPS analyses are consistent with theoretical calculation that sulfoxide sites can be regarded as typical donor sites, while thioether sites can be regarded as acceptor sites upon adsorption of LiO_2*/Li_2O_2. The differential capacity versus voltage plots (dQ/dV) of different electrodes are utilized to distinguish the redox behavior induced by charge transport from the capacitance behavior mainly induced by mass transport (Figs. S18 and 19). The dQ/dV plots of PABSA/LDO-600 exhibit no distinct oxidation peak upon cycling (Fig. S18), while the dQ/dV plots of PAN/LDO-700 show the shift of oxidation and reduction peaks toward higher and lower potential upon cycling, respectively (Fig. S19a). The redox peaks of PAN/LDO-700 disappear after 70 cycles. The dQ/dV plots of PAN/LDO-700 reveal distinct capacitive behavior upon cycling. Cycled at a fixed capacity of 0.53 mAh cm^{-2}, the dQ/dV plots of PABSA/LDO-700 show distinct reduction and oxidation peaks upon cycling, indicative of the presence of charge transport in (dis)charged PABSA/LDO-700 (Fig. S19b). The enhanced charge transport on discharged PABSA/LDO-700 is further demonstrated by electrochemical impedance spectroscopy (EIS) analyses (Fig. 5). The Z′ intersection at high frequency denotes the ohmic resistance. The diameter of the semicircle is associated with the charge transfer resistance. The ohmic resistance of initial PABSA/LDO-700, PABSA/LDO-600 and PABSA/LDO-300 exhibits an insignificant difference. However, the charge transfer resistance of PABSA/LDO-700 is lower than that of PABSA/LDO-600 and PABSA/LDO-300. After discharge, the increase of charge-transfer resistance of discharged PABSA/LDO-700 is much less than that of discharged PABSA/LDO-600 and PABSA/LDO-300. Relative element fitting parameters in equivalent circuit are detailed in Table S4.

The oxygen reduction in Li–O_2 batteries is generally believed to experience two different processes, *i.e.*, "surface" or "solvated" process [26,44]. The film-like Li_2O_2 with quasi-amorphous nature is generally believed to form via surface process, while the toroid-like crystalline Li_2O_2 generates through the chemical disproportionation of LiO_2* in solvated process [44,51,52]. The surface process is similar with the

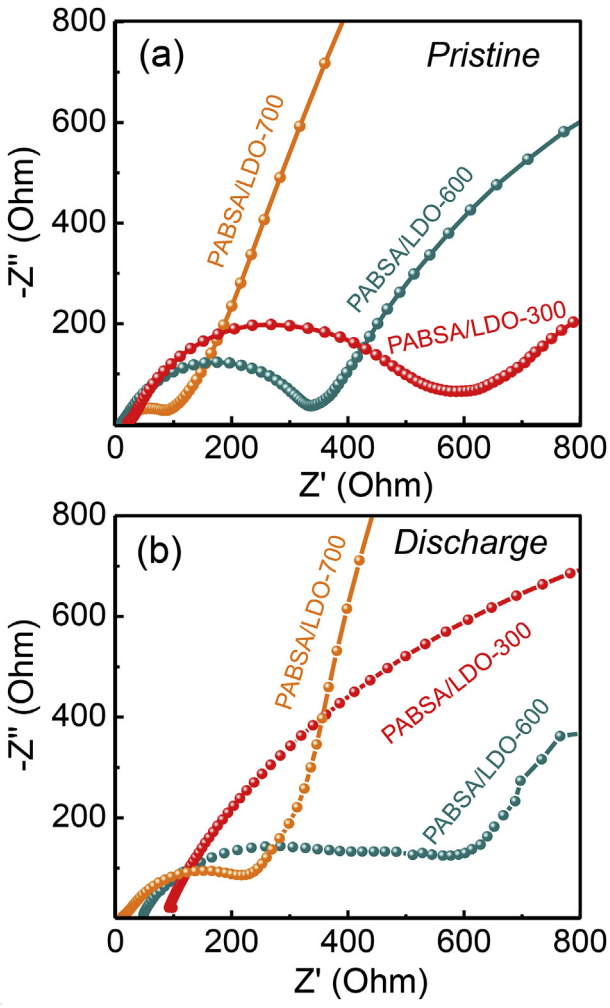

Fig. 5. EIS Nyquist plots of PABSA/LDO-300, PABSA/LDO-600 and PABSA/LDO-700 (a) before and (b) after first discharge.

electrodeposition, the reaction of O_2 and Li^+ to deposit Li_2O_2 on the electrode surface. The solvated process involves the disproportionation of LiO_2* in the electrolyte to form Li_2O_2. Theoretically, the nuclei of LiO_2*/Li_2O_2 over the critical size under a certain cathodic polarization can be stabilized, while the nuclei that cannot reach the critical size will dissociate into the electrolyte. The relationship of the overpotential and the critical size complies with the following equation.

$$r_c = \frac{\sigma}{\rho F \eta} M_{Li_2O_2 \ or \ LiO_2} \quad (1)$$

where η is the overpotential on activated sites in reduction; F: Faraday constant; ρ is the density of deposited LiO_2*/Li_2O_2 nuclei; σ is interfacial tension between nuclei and electrolyte.

According to Eq. (1), the lower the cathodic overpotential, the larger the critical size is and consequently more LiO_2*/Li_2O_2 would be solvated into the electrolyte. The formation of discharge products with different sizes and morphologies might be associated with the shift of the electric double-layer potential on the cathode surface, and the supersaturation of LiO_2*/Li_2O_2 in the electrolyte originated from different preferential adsorption of reactants and intermediates on acceptor and donor sites.

Acceptor sites, such as S3 and S4 sites are inclined to interact with Li and withdraw electrons from adsorbed Li_2O_2 to induce the formation of Li_2O_2 discharge products with Li vacancies or small hole polarons as charge carriers (A-$Li_{2-x}O_2$). The surface of A-$Li_{2-x}O_2$ is inclined to further specifically adsorb LiO_2* and Li_2O_2. The specific adsorption of LiO_2*/Li_2O_2 on the surface with an emerging diffuse layer potential (ψ) between the Stern plane and the bulk of the electrolyte might induce the decrease of the electric double layer potential and the increase of overpotential on the acceptor sites [53]. The increase of overpotential would induce faster nucleation rate of solvated LiO_2*/Li_2O_2 on the acceptor sites. The relationship of the overpotential and the nucleation rate complies with the following equation. Relative derivation based on the Kossel, Stranski and Volmer (KSV) crystal nucleation theory is detailed in Supporting Information.

$$\omega = K \exp\left(-\frac{M_{Li_2O_2 \ or \ LiO_2} \pi h \sigma^2 L}{\rho F R T \eta}\right) \quad (2)$$

where ω is the nucleation rate; K is pre-exponential factor; h is the molecule size of LiO_2*/Li_2O_2; L is Avogadro constant value.

According to crystal nucleation and growth, high nucleation rate would lead to the deposition of Li_2O_2 particles with small size. As precipitation goes on, the activated sites would be gradually covered and isolated by discharge products, which might lead to the gradual inhibition of the surface reduction of A-$Li_{2-x}O_2$. Meanwhile, the supersaturation of solvated LiO_2*/Li_2O_2 in electrolyte might decrease with the gradual increase of overpotential. At low supersaturation, the crystal growth rate is faster than the nucleation rate. Subsequent precipitation of LiO_2*/Li_2O_2 from electrolyte would result in the growth of nuclei and the formation of protrusion on the surface of A-$Li_{2-x}O_2$. The tip of the protrusion with considerably high electric field might result in further growth of the protrusion to form large needle-like or flaky discharge product (Fig. 6a). This might explain the presence of flaky discharge products with embedded particles on discharged PABSA/LDO-700 (Fig. 4a and Fig. S20).

Donor sites, such as S2 sites tend to interact with reactive oxygen species and donate electrons to adsorbed Li_2O_2 to induce the formation of Li_2O_2 with small electron polarons or disordered Li_2O_2 structure as charge carriers (D-Li_2O_2). The barrier for oxygen-vacancy diffusion in Li_2O_2 (1.5 eV) is too high to form Li_2O_{2-x} [19]. The surface of D-Li_2O_2 with negative charge tends to adsorb Li^+ and O_2, favorable for surface reduction to generate LiO_2*/Li_2O_2. If the activated sites have strong affinity to O_2, the full coverage of O_2 on donor sites might lead to the substantial decrease of the electric double-layer potential and the increase of overpotential. In low electric double-layer potential on donor sites (large overpotential or O_2 coverage), according to Eq. (2), nucleation rate of LiO_2*/Li_2O_2 on donor sites is high (Fig. 6b). It is prone to deposit film-like discharge products composed of small nuclei on cathode surface, which is consistent with the formation of film-like Li_2O_2 on noble metal by surface process instead of disproportionation in the solvated

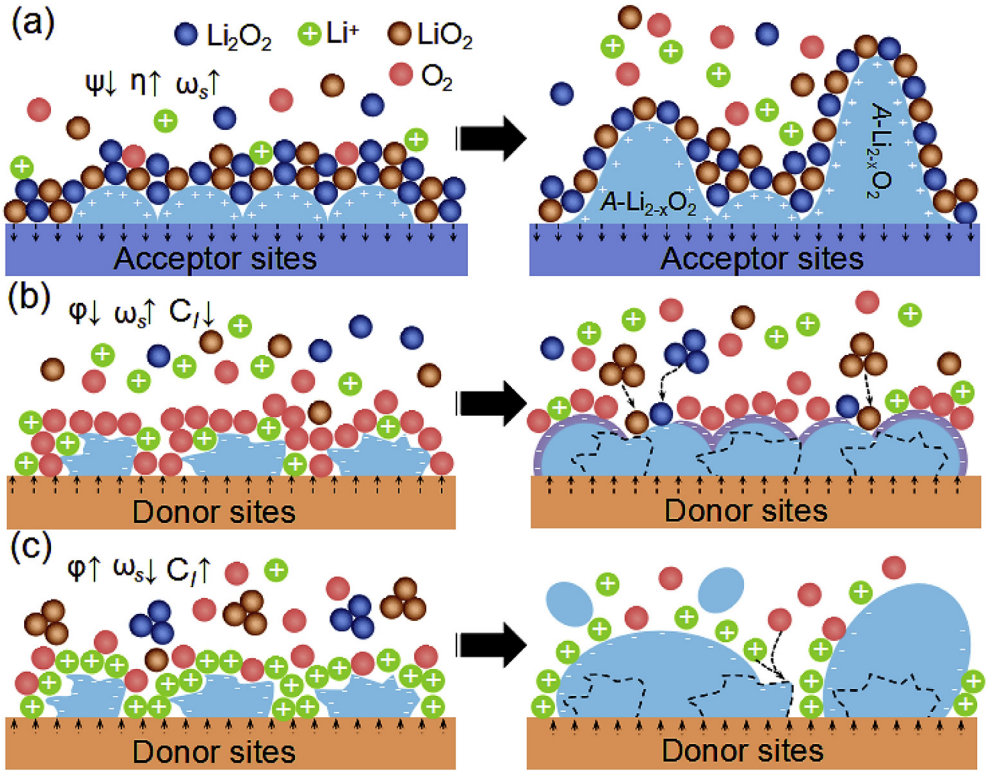

Fig. 6. The feasible mechanism based on KSV crystal nucleation theory to explain the relationship between the "surface" and the "solvated" process, *i.e.*, how the disproportionated products precipitate onto the catalyst surface and how the solid products originated from surface reaction escape from the catalyst surface on (a) acceptor sites, (b) donor sites with large overpotential or O_2 coverage, (c) donor sites with low overpotential or small O_2 coverage. Ψ: diffuse-layer potential; η: overpotential; ω_s: nucleation rate; C_l: the supersaturation of dissolved LiO_2*/Li_2O_2 in electrolyte.

process [23,54–56]. Moreover, the supersaturation of dissolved LiO_2*/-Li_2O_2 in electrolyte is relatively low, which would result in faster crystal growth rate than nucleation rate. Successive precipitation of Li_2O_2 in the electrolyte would deposit onto the generated nuclei on the surface. In contrast, in large electric double-layer potential on donor sites (low overpotential or O_2 coverage), large particles are apt to generate on the surface and small nuclei are prone to generate by disproportionation in the solvated process (Fig. 6c). It is consistent with the reported potential-dependent morphology of Li_2O_2 during potentiostatic discharge [49,57], *i.e.*, small particles of Li_2O_2 formed at low discharge voltage (large η) while large toroid formed at high discharge voltage (low η), and the electron transport relevant morphology evolution, *i.e.*, CoN with fast electron transport (low η) generated large complete toroid Li_2O_2, while Co_3O_4 with slow electron transport generated toroid composed of Li_2O_2 particles with small size [26].

Li_2O_2 deposited on donor sites tends to gain extra electrons. The extra electrons in the Li_2O_2 crystal would fill up localized O_2^{3-} to form small electron polarons. Electron transport in Li_2O_2 on donor sites by small electron polarons hopping from O_2^{2-} to another O_2^{2-} is necessary to overcome the barrier of 0.5–1 eV [15,16]. However, the migration barrier of the hole polarons on acceptor sites is only 0.1–0.2 eV [17], which is much smaller than that of electron polarons on donor sites. Therefore, deposition of Li_2O_2 on acceptor sites with small hole polarons as charge carriers is more favorable for charge transport in discharge products than that on donor sites with small electron polarons as charge carriers.

6. Conclusions

In conclusion, rational surface engineering of cathode catalysts with donor and acceptor sites to improve catalyst/discharge products interfacial electron transfer is promising to enhance charge transport in discharge products and accelerate reaction kinetics for effectively catalyzing Li_2O_2 formation and decomposition. By pyrolysis of PABSA at different temperatures, the donor and acceptor sites are constructed by regulating different sulfur sites on carbon nanosheets. Thioether (S3) and polysulfide (S4) sites formed at carbonized temperature over 700 ºC are prone to accept electrons from Li^+ in lithium oxides upon adsorbing LiO_2*/Li_2O_2, while sulfoxide (S2) sites generated through the incomplete decomposition of sulfonate groups at relatively low temperature tend to donate electrons to adsorbed reactive oxygen species. PABSA/LDO-600 with S2 sites but without S3 and S4 sites operated in O_2 exhibits slope-like (dis)charge profiles, while PABSA/LDO-700 with hybrid S2, S3 and S4 sites exhibits distinct (dis)charge voltage plateau. Analysis of the generated disc-like particles and flakes on discharged PABSA/LDO-700 reveals the existence of abundant defects such as vacant sties, lattice distortion and amorphous structure. Further observation of the generated large granules on discharged PABSA/LDO-600 reveals the existence of amorphous phase on the outside surface. The perspectives of the development of cathode catalysts with optimized donor and acceptor sites are proposed to tailor deposition of Li_2O_2 discharge products with enhanced defective charge transport for high-performance Li–O_2 batteries.

Declaration of competing interest

There is no conflict of interest to declare.

Acknowledgements

This work was financially supported by the National Natural Science Foundation of China (21871177, 21673140, 21720102002), the Opening Project of State Key Laboratory of High Performance Ceramics and Superfine Microstructure (SKL201703SIC). The authors thank Prof. Pan Liu (School of Materials Science and Engineering, SJTU) for assistant with Cs-corrected STEM characterization, Dr. Xue Ding (Instrumental Analysis Center, SJTU) for assistant with XPS characterization and Shanghai Synchrotron Radiation Facility for the beam time (BL14W1).

Appendix A. Supplementary data

Supplementary data to this article can be found online at https://doi.org/10.1016/j.ensm.2019.10.032.

References

[1] D. Wang, X. Mu, P. He, H. Zhou, Mater. Today 26 (2019) 87–99, https://doi.org/10.1016/j.mattod.2019.01.016.
[2] J. Lu, L. Li, J.-B. Park, Y.-K. Sun, F. Wu, K. Amine, Chem. Rev. 114 (2014) 5611–5640.
[3] H.-D. Lim, B. Lee, Y. Bae, H. Park, Y. Ko, H. Kim, J. Kim, K. Kang, Chem. Soc. Rev. 46 (2017) 2873–2888.
[4] Z. Lyu, Y. Zhou, W. Dai, X. Cui, M. Lai, L. Wang, F. Huo, W. Huang, Z. Hu, W. Chen, Chem. Soc. Rev. 46 (2017) 6046–6072.
[5] K.X. Wang, Q.C. Zhu, J.S. Chen, Small (2018) 1800078.
[6] C. Wang, Z. Xie, Z. Zhou, APL Mater. 7 (2019) 40701.
[7] P. Zhang, Y. Zhao, X. Zhang, Chem. Soc. Rev. 47 (2018) 2921–3004.
[8] Z. Ma, X. Yuan, L. Li, Z.-F. Ma, D.P. Wilkinson, L. Zhang, J. Zhang, Energy Environ. Sci. 8 (2015) 2144–2198.
[9] M.D. Radin, D.J. Siegel, Energy Environ. Sci. 6 (2013) 2370–2379.
[10] V. Viswanathan, K.S. Thygesen, J. Hummelshøj, J.K. Nørskov, G. Girishkumar, B. McCloskey, A. Luntz, J. Chem. Phys. 135 (2011) 214704.
[11] Y.-C. Lu, Y. Shao-Horn, J. Phys. Chem. Lett. 4 (2012) 93–99.
[12] J. Højberg, B.D. McCloskey, J. Hjelm, T. Vegge, K. Johansen, P. Norby, A.C. Luntz, ACS Appl. Mater. Interfaces 7 (2015) 4039–4047.
[13] M.D. Radin, C.W. Monroe, D.J. Siegel, J. Phys. Chem. Lett. 6 (2015) 3017–3022.
[14] O. Gerbig, R. Merkle, J. Maier, Adv. Mater. 25 (2013) 3129–3133.
[15] J. Kang, Y.S. Jung, S.-H. Wei, A.C. Dillon, Phys. Rev. B 85 (2012) 035210.
[16] J.M. Garcia-Lastra, J.S. Myrdal, R. Christensen, K.S. Thygesen, T. Vegge, J. Phys. Chem. C 117 (2013) 5568–5577.
[17] S.P. Ong, Y. Mo, G. Ceder, Phys. Rev. B 85 (2012) 081105.
[18] A.C. Luntz, V. Viswanathan, J. Voss, J. Varley, J. Nørskov, R. Scheffler, A. Speidel, J. Phys. Chem. Lett. 4 (2013) 3494–3499.
[19] M.D. Radin, C.W. Monroe, D.J. Siegel, Chem. Mater. 27 (2015) 839–847.
[20] Y. Wang, Z. Liang, Q. Zou, G. Cong, Y.-C. Lu, J. Phys. Chem. C 120 (2016) 6459–6466.
[21] W.B. Luo, X.W. Gao, D.Q. Shi, S.L. Chou, J.Z. Wang, H.K. Liu, Small 12 (2016) 3031–3038.
[22] M. Lee, Y. Hwang, K.-H. Yun, Y.-C. Chung, J. Power Sources 288 (2015) 296–301.
[23] X. Luo, L. Ge, L. Ma, A.J. Kropf, J. Wen, X. Zuo, Y. Ren, T. Wu, J. Lu, K. Amine, Adv. Energy Mater. (2018) 1703230.
[24] J. Lu, L. Cheng, K.C. Lau, E. Tyo, X. Luo, J. Wen, D. Miller, R.S. Assary, H.-H. Wang, P. Redfern, Nat. Commun. 5 (2014) 4895.
[25] J. Zhu, X. Ren, J. Liu, W. Zhang, Z. Wen, ACS Catal. 5 (2014) 73–81.
[26] S.-M. Xu, Q.-C. Zhu, M. Harris, T.-H. Chen, C. Ma, X. Wei, H.-S. Xu, Y.-X. Zhou, Y.-C. Cao, K.-X. Wang, Nano Lett. 16 (2016) 5902–5908.
[27] C. Shu, B. Li, B. Zhang, D. Su, ChemSusChem 8 (2015) 3973–3976.
[28] J. Shui, F. Du, C. Xue, Q. Li, L. Dai, ACS Nano 8 (2014) 3015–3022.
[29] Y. Jing, Z. Zhou, ACS Catal. 5 (2015) 4309–4317.
[30] H. Jiang, T. Zhao, L. Shi, P. Tan, L. An, J. Phys. Chem. C 120 (2016) 6612–6618.
[31] X. Ren, B. Wang, J. Zhu, J. Liu, W. Zhang, Z. Wen, Phys. Chem. Chem. Phys. 17 (2015) 14605–14612.
[32] G. Kresse, J. Furthmüller, Phys. Rev. B 54 (1996) 11169.
[33] G. Kresse, J. Furthmüller, Comput. Mater. Sci. 6 (1996) 15–50.
[34] S.-M. Xu, Z.-C. Ren, X. Liu, X. Liang, K.-X. Wang, J.-S. Chen, Energy Storage Mater 15 (2018) 291–298.
[35] M. Wei, X. Tian, J. He, M. Pu, G. Rao, H. Yang, L. Yang, T. Liu, D.G. Evans, X. Duan, Eur. J. Inorg. Chem. 2006 (2006) 3442–3450.
[36] R.F. Bader, Chem. Rev. 91 (1991) 893–928.
[37] W. Tang, E. Sanville, G. Henkelman, J. Phys. Condens. Matter 21 (2009) 084204.
[38] G. Wu, K.L. More, C.M. Johnston, P. Zelenay, Science 332 (2011) 443–447.
[39] A. Zitolo, N. Ranjbar-Sahraie, T. Mineva, J. Li, Q. Jia, S. Stamatin, G.F. Harrington, S.M. Lyth, P. Krtil, S. Mukerjee, Nat. Commun. 8 (2017) 957.
[40] Y. Tsao, Z. Chen, S. Rondeau-Gagne, Q. Zhang, H. Yao, S. Chen, G. Zhou, C. Zu, Y. Cui, Z. Bao, ACS Energy Lett 2 (2017) 2454–2462.
[41] J. Liang, Y. Jiao, M. Jaroniec, S.Z. Qiao, Angew. Chem. Int. Ed. 124 (2012) 11664–11668.
[42] B. Sun, X. Huang, S. Chen, P. Munroe, G. Wang, Nano Lett. 14 (2014) 3145–3152.
[43] S.M. Xu, Q.C. Zhu, J. Long, H.H. Wang, X.F. Xie, K.X. Wang, J.S. Chen, Adv. Funct. Mater. 26 (2016) 1365–1374.
[44] L. Johnson, C. Li, Z. Liu, Y. Chen, S.A. Freunberger, P.C. Ashok, B.B. Praveen, K. Dholakia, J.-M. Tarascon, P.G. Bruce, Nat. Chem. 6 (2014) 1091.
[45] J. Lu, Y.J. Lee, X. Luo, K.C. Lau, M. Asadi, H.-H. Wang, S. Brombosz, J. Wen, D. Zhai, Z. Chen, Nature 529 (2016) 377.
[46] H.-D. Lim, Y.S. Yun, Y. Ko, Y. Bae, M.Y. Song, H.J. Yoon, K. Kang, H.-J. Jin, Carbon 118 (2017) 114–119.
[47] S.M. Xu, X. Liang, Z.C. Ren, K.X. Wang, J.S. Chen, Angew. Chem. Int. Ed. 130 (2018) 6941–6945.
[48] J. Yang, D. Zhai, H.-H. Wang, K.C. Lau, J.A. Schlueter, P. Du, D.J. Myers, Y.-K. Sun, L.A. Curtiss, K. Amine, Phys. Chem. Chem. Phys. 15 (2013) 3764–3771.
[49] B.M. Gallant, D.G. Kwabi, R.R. Mitchell, J. Zhou, C.V. Thompson, Y. Shao-Horn, Energy Environ. Sci. 6 (2013) 2518–2528.

[50] R.R. Mitchell, B.M. Gallant, Y. Shao-Horn, C.V. Thompson, J. Phys. Chem. Lett. 4 (2013) 1060–1064.
[51] W.-J. Kwak, J.-B. Park, H.-G. Jung, Y.-K. Sun, ACS Energy Lett 2 (2017) 2756–2760.
[52] E. Yilmaz, C. Yogi, K. Yamanaka, T. Ohta, H.R. Byon, Nano Lett. 13 (2013) 4679–4684.
[53] F. Hingston, R. Atkinson, A. Posner, J. Quirk, Nature 215 (1967) 1459.
[54] H.-D. Lim, H. Song, H. Gwon, K.-Y. Park, J. Kim, Y. Bae, H. Kim, S.-K. Jung, T. Kim, Y.H. Kim, Energy Environ. Sci. 6 (2013) 3570–3575.
[55] Y. Yang, T. Zhang, X. Wang, L. Chen, N. Wu, W. Liu, H. Lu, L. Xiao, L. Fu, L. Zhuang, ACS Appl. Mater. Interfaces 8 (2016) 21350–21357.
[56] Y. Zhang, X. Zhang, J. Wang, W.C. McKee, Y. Xu, Z. Peng, J. Phys. Chem. C 120 (2016) 3690–3698.
[57] L. Wang, Y. Zhang, Z. Liu, L. Guo, Z. Peng, Green Energy Environ 2 (2017) 186–203.